Meeting of the International Geological Correlation Programme No. 262, Cretaceous Facies in Orogenic Belts (Athens, Greece), p. 4 (abstr.) (1992).
19. R. Coccioni *et al.*, *Boll. Soc. Geol. Ital.* **106**, 183 (1987).
20. R. Coccioni *et al.*, in *Cretaceous of the Western Tethys*, J. Wiedmann, Ed. (Lubrecht and Cramer, Forestburgh, NY, 1990), pp. 563–584.
21. W. V. Sliter, *Geology* **17**, 909 (1989).
22. F. Robaszynski, *Geobios* **11**, 311 (1988).
23. J. A. Tarduno *et al.*, *Science* **254**, 399 (1991).
24. M. A. Arthur and I. Premoli Silva, in *Nature and Origin of Cretaceous Carbon-Rich Facies*, S. O. Schlanger and M. B. Cita, Eds. (Academic Press, New York, 1982), pp. 7–54.
25. S. O. Schlanger *et al.*, *Geol. Soc. Am. Spec. Pap.* **26**, 371 (1987).
26. M. A. Arthur, W. E. Dean, L. M. Pratt, *Nature* **335**, 714 (1988).
27. B. Schmitz, G. Aberg, L. Werdelin, P. Forey, S. V. Bendix-Almgreen, *Geol. Soc. Am. Bull.* **103**, 786 (1991).
28. F. M. Richter and D. J. DePaolo, *Earth Planet. Sci. Lett.* **83**, 27 (1987).
29. The $^{87}Sr/^{86}Sr$ ratios in fish teeth from a Miocene volcano-sedimentary clay in the northeastern Apennines are consistent with the bulk ratios for carbonate of adjacent limestones overlying and underlying the clay layer, whereas the $^{87}Sr/^{86}Sr$ ratios of recrystallized foraminiferal tests have been shifted [A. Montanari *et al.*, *Newsl. Stratigr.* **23**, 151 (1991)].
30. Each sample was composed of 2 to 10 teeth, weighing from 0.1 to 0.5 mg. The fish teeth samples were dissolved in 4 N nitric acid. One aliquot was passed through an ion exchange column to separate Sr from other elements, and the $^{87}Sr/^{86}Sr$ ratio measurements were made on a VG Sector-354 mass spectrometer (Fisons Instruments, United Kingdom) in dynamic multicollection mode [see B. L. Ingram, thesis, Stanford University (1992)]. Each sample was measured in duplicate. The other aliquot was spiked with ^{84}Sr, ^{85}Rb, ^{145}Nd, and ^{152}Sm to determine Sr, Rb, Nd, and Sm concentrations by isotope dilution. The Sr standards used were the U.S. Geological Survey EN-1 *Tridacna* shell for modern seawater and the NBS-987 Sr standard, with $^{87}Sr/^{86}Sr$ ratios of 0.709189 and 0.710275, respectively. The $^{87}Sr/^{86}Sr$ ratios were normalized to seawater standard as follows: $\Delta^{87}Sr = (^{87}Sr/^{86}Sr_{sample} - {}^{87}Sr/^{86}Sr_{standard}) \times 10^5$. The uncertainty of each $^{87}Sr/^{86}Sr$ ratio measurement (2σ) is $\pm 1 \times 10^{-5}$, or ± 1 $\Delta^{87}Sr$ unit.
31. It has been demonstrated that postdepositional recrystallization of ancient fish teeth causes an increase in crystallinity and carbonate content and a decrease in Sr content (those samples with the highest crystallinity index had Sr concentrations below 2000 ppm). A. Shemesh, *Geochim. Cosmochim. Acta* **54**, 2433, (1990).
32. The black shale sediments are thought to be deposited during warm, greenhouse climates [H. Weissert and A. Lini, in *Controversies in Modern Geology*, D. W. Muller, J. A. McKenzie, H. Weissert, Eds. (Academic Press, New York, 1991), pp. 173–191].
33. R. L. Larson, *Geology* **19**, 547 (1991).
34. R. L. Larson, *ibid.*, p. 963.
35. M. F. Coffin and O. Eldholm, *Rev. Geophys.* **19**, 1 (1994).
36. M. A. Richards, D. L. Jones, R. A. Duncan, D. J. DePaolo, *Science* **254**, 263 (1991).
37. T. W. Donnelly, K. Melson, R. Kay, J. J. W. Rogers, *Init. Rep. Deep Sea Drill. Proj.* **15**, 989 (1973).
38. J. Sigal, *Géol. Mediterr.* **4**, 99 (1977).
39. W. B. Harland *et al.*, *A Geologic Time Scale 1989* (Cambridge Univ. Press, Cambridge, 1990), pp. 1–263.
40. T. D. Herbert and A. G. Fischer, *Nature* **321**, 739 (1986).
41. B. Beaudoin and E. M'Ban, in *Proceedings of the 29th International Geology Congress*, Kyoto, Japan, 1992 (abstr.), vol. 2/3, p. 291.
42. We thank S. C. Brassell, J. C. Ingle, M. McWilliams, Y. Kolodny, and M. Chambers for helpful reviews of the manuscript and D. J. DePaolo for use of his laboratory at the Center of Isotope Geochemistry at the University of California, Berkeley. This work was started as the doctoral thesis of B.L.I. at Stanford University and was supported by the Petroleum Research Fund (B.L.I.), the Ministero Universitario della Ricerca Scientifica e Tecnologica (MURST) of Italy (R.C.), and National Science Foundation grant EAR-91059297 and Exxon Production Research (A.M.).

17 December 1993; accepted 15 March 1994

Origin of Saturn's E Ring: Self-Sustained, Naturally

Douglas P. Hamilton* and Joseph A. Burns†‡

Saturn's diffuse E ring spans the region between 3 and 8 saturnian radii (R_S), has its peak brightness near the orbit of the satellite Enceladus (3.95 R_S), and is thought to be composed primarily of icy particles 1.0 ± 0.3 micrometers in radius. Such particles are shown to move periodically along highly elliptical paths that cross the orbits of several saturnian satellites; the resulting energetic collisions of E ring particles with embedded satellites are capable of sustaining the E ring at its current optical depth. With several reasonable assumptions, this model naturally selects Enceladus as the primary source of ring material and may also provide mechanisms that explain the generation of the unusual amount of submicrometer dust in the neighboring F and G rings, the excess of OH molecules observed within the E ring, and the orbital brightness variations of nearby satellites.

The radial distribution, radial extent, and three-dimensional structure of Saturn's E ring (*1*) are consistent with the orbital dynamics of micrometer-sized particles injected at Enceladus (*2*, *3*). Such particles move along paths that periodically become highly elliptical, instead of remaining circular as typically assumed (Fig. 1).

All bodies orbiting Saturn are perturbed by the planet's significant equatorial bulge, which causes elliptical orbits to precess in space while retaining their size and shape. Micrometer-sized dust grains are additionally influenced by strong nongravitational forces, principally electromagnetism and solar radiation pressure. The former arises because objects near Saturn invariably acquire negative electric potentials by sweeping up magnetospheric electrons and ions (*2*). Movement of these charged grains through Saturn's rotating magnetic field (*4*) causes a Lorentz force (*2*, *3*), the primary consequence of which is orbital regression (that is, elliptic orbits rotate in the direction opposite to that induced by oblateness; as before, the orbital size and shape are unaltered). Finally, small grains are measurably perturbed by solar radiation pressure, which is directed radially away from the sun (*5*); unlike the previously mentioned perturbations, radiation pressure induces a periodic variation in orbital eccentricity. The amplitude of this eccentricity oscillation is inversely proportional to the orbital precession rate (*2*).

When all these perturbations act simultaneously on E ring grains 1 μm in radius, precession from oblateness nearly cancels regression from the Lorentz force, allowing eccentricities to become appreciable (Fig. 2). The orbits of bigger (and smaller) particles precess (or regress) rapidly enough that radiation pressure cannot induce such large eccentricities (Fig. 2).

Because orbits transform from circles to ellipses and back again in just a few years (Fig. 2), micrometer-sized material, even if introduced on a nearly circular path, swiftly covers a broad, flattened torus (Fig. 1). The spatial distribution of grains that have undergone such orbital changes after being launched from Enceladus roughly matches (i) the observed radial profile of the E ring, (ii) the density peak centered on that satellite (*2*), and (iii) the observed vertical structure (*3*). This close correspondence between the model and reality suggests that Enceladus is the primary source of E ring material; moreover, the fit to the E ring's radial and vertical profiles is further improved if Tethys contributes additional material (*3*).

The E ring shares the region between 3 and 8 R_S with an ensemble of moons that travel along nearly circular paths (Table 1); consequently, whenever the orbits of E ring particles become moderately eccentric, they cross the paths of these satellites (Fig. 2). Given a satellite of radius R_{moon} on a low-eccentricity orbit at radial distance a_{moon}, a grain on a "crossing" orbit will strike the moon with an *e*-folding collisional time scale

Astronomy Department, Cornell University, Ithaca, NY 14853, USA.

*Present address: Max Planck Institut für Kernphysik, Heidelberg, Germany.
†Also at Theoretical and Applied Mechanics, Cornell University, Ithaca, NY 14853, USA.
‡To whom correspondence should be addressed.

$$T_{col} \approx \pi(\sin^2 i_{dust} + \sin^2 i_{moon})^{1/2} \left(\frac{a_{moon}}{R_{moon}}\right)^2 \left(\frac{U_r}{U}\right) T_{orb} \quad (1)$$

where $T_{orb} = 2\pi a_{dust}/v_{dust}$ is the dust grain's orbital period, a_{dust} is its semimajor axis, v_{dust} is its orbital velocity (6), U is the relative velocity between the moon and the dust grain, U_r is its radial component, and the orbital inclinations i_{dust} and i_{moon} (Table 1) are measured relative to the planet's equatorial plane. The ratio U_r/U is nearly independent of e_{dust} and, to within <20%, equals one.

The grain-moon collision time scales in Table 1 are very rapid: Enceladus, immersed in the heart of the E ring, can sweep up the extant ring in about 20 years. Without a recent supply of new material, the E ring should have lost more than half its particles in the interval between its discovery (*7*) in 1966 and the Voyager flybys in 1981. Because it is unlikely that the E ring is disappearing so quickly, a mechanism that continuously replenishes the ring must exist. In contrast, a burst of activity in the distant past—through volcanism (*8*), geysers (*9*), or large impacts (*10*)—is incapable of accounting for the E ring observed today: Whatever process creates E ring particles must be occurring now.

Grain-moon collisions are commonplace, happen continuously, and because of highly eccentric dust orbits, are quite energetic. The relative speed between a particle traveling on a low-inclination, arbitrarily sized eccentric orbit and a moon moving along a circular, nearly equatorial path is about

$$v_{col} \approx e v_{moon} \quad (2)$$

where v_{moon}, the orbital speed of the moon, is roughly 10 km/s (Table 1). This simple expression is accurate to about 10% for particle orbits of all sizes and shapes, as long as the collision does not occur near an orbital turning point (Fig. 1). Owing to the large eccentricities of E ring grains, collision velocities often surpass 5 km/s, a value far in excess of satellite escape velocities (Table 1). These hypervelocity impacts send an amount of mass greatly exceeding that of the impactor (*11*) into circumsaturnian orbit where the ejected material merges with the E ring.

Because micrometer-sized impacts add material to the E ring, the ring may sustain itself with these collisions. However, only a small fraction of the collisional ejecta is composed of the dynamically favored, micrometer-sized grains. Grains that fall outside this special size window never attain the high eccentricities necessary for the most energetic collisions (Fig. 2); instead, they eventually encounter their source satellite in low-velocity collisions that liberate little or no mass. Thus, a self-sustaining E ring requires that, on average, the collision of a micrometer-sized grain must eject at least one micrometer-sized fragment.

Because the collisional fragments of interest are similar in size to the projectile and they must survive intact, spallation (*12*) is suggested. A few experiments (*13–15*), in which small hypervelocity (2 to 10 km/s) projectiles collide with icy targets, yield large, rapidly moving spall fragments. These experiments, however, give inconclusive answers to the issue at hand because the fastest projectile-sized collisional fragments have speeds similar to Enceladus' escape velocity.

If a typical collision of a micrometer-sized E ring grain with an embedded satellite produces more than one micrometer-sized ejecta fragment, then particles are added to the system at a rate proportional to N, the number of ring members. Intragrain collisions, which occur at a rate $\sim N^2$ and (by assumption) lead to catastrophic fragmentation and vaporization, eventually stem this otherwise exponential growth and stabilize the ring at a particular optical depth. If the E ring is self-sustaining, generation by impact must balance loss through mutual collision. If a typical grain-moon collision produces only a few new grains, then at steady state, such impacts and grain-grain collisions should occur with roughly similar probabilities; this appears to be the case for the actual E ring. Put another way, the known grain-moon and grain-grain collision rates allow us to estimate the E ring's steady-state optical depth; as discussed below, this calculation yields a number that is within a factor of 3 of the correct value.

Several independent observations also lend support to the idea of a self-sustaining E ring. The albedo patterns of the saturnian satellites are consistent with the fact that eccentrically orbiting E ring grains commonly strike these moons (*16*). Furthermore, the fact that Enceladus itself is photometrically similar across diverse geologic

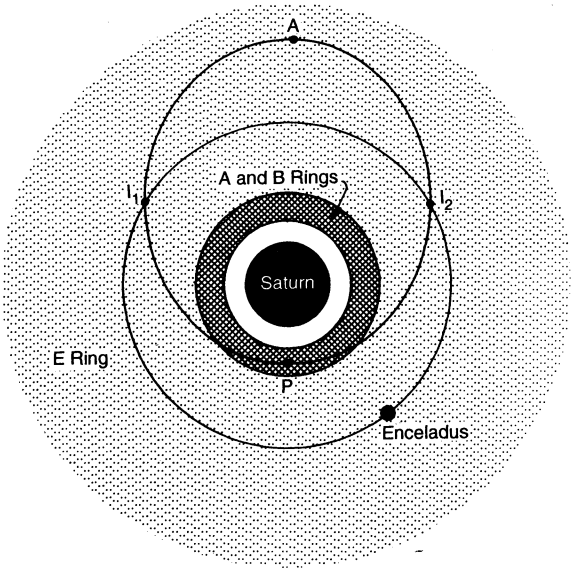

Fig. 1. The saturnian system. The E ring (stippled) is external to the optically thick A and B rings and encompasses the orbits of four major saturnian satellites: Mimas, Enceladus, Tethys, and Dione (Table 1). For clarity, we show only Enceladus' path (the circle of radius $a_{moon} \sim 3.95 R_S$) and that of an E ring grain that originated on Enceladus (ellipse with semimajor axis $a_{dust} = 3.95\ R_S$ and ellipticity $e_{dust} = 0.5$). The turning points A (apocenter) and P (pericenter) of the particle's orbit are located at distances $a_{dust}(1 + e_{dust})$ and $a_{dust}(1 - e_{dust})$ from Saturn. The E ring particles cross the orbit of Enceladus at the points I_1 and I_2 and can venture within the radial distance of the opaque main rings only by flying above or below them.

Table 1. Orbital and physical properties of saturnian satellites within Saturn's E ring (*27*): orbital semimajor axes, eccentricities, and inclinations; satellite radii and densities; escape speeds from satellite surfaces ($v^2_{escape} = 2GM_{moon}/R_{moon}$, where M is mass and G is the universal gravity constant) and circular orbital speeds ($v^2_{moon} = GM_{Saturn}/a_{moon}$; $M_{Saturn} = 5.688 \times 10^{29}$ g); and the results from Eq. 1. The densities of the leading and trailing Lagrangian companions of Tethys (T+,T−) and the leading companion of Dione (D+) are unmeasured.

Name	a_{moon} (R_S)	e_{moon}	i_{moon} (degrees)	R_{moon} (km)	ρ_{moon} (g/cm^3)	v_{escape} (km/s)	v_{moon} (km/s)	T^*_{col} (years)
Mimas	3.08	0.02	1.53	195	1.17	0.16	14.3	200
Enceladus	3.95	0.00	0.02	250	1.24	0.21	12.6	19
Tethys	4.89	0.00	1.09	525	1.26	0.44	11.4	98
Telesto (T+)	4.89	0.00	0.00	12	(1.0)	0.009	11.4	17,000
Calypso (T−)	4.89	0.00	0.00	12	(1.0)	0.009	11.4	17,000
Dione	6.26	0.00	0.02	560	1.44	0.50	10.0	19
Helene (D+)	6.26	0.01	0.20	16	(1.0)	0.012	10.0	51,000
Rhea	8.74	0.00	0.35	765	1.33	0.66	8.5	120

*Assumes, for illustrative purposes, that $i_{dust} = 0.1°$ and $a_{dust} = a_{moon}$.

zones suggests the presence of a ubiquitous surface layer of micrometer-sized grains (*17*), perhaps as a result of a long history of sandblasting by E ring material.

Energetic grain-moon collisions are also indicated by the copious amount of OH observed in the E ring region, which seems to be 20 times more than traditional sources (for example, micrometeoroid bombardment and sputtering) can supply (*18*). The collisions that we have argued are capable of lofting a micrometer-sized object into space liberate many times that much mass in the form of water molecules and tiny aggregates. The mass flux of E ring grains onto Enceladus exceeds the interplanetary flux [taken to be 4.5×10^{-17} g/cm^2 per second (*19*)] by 10^4; even after accounting for the higher speeds of the latter, the E ring source is still about 100 times more efficient and may generate the observed population of OH molecules (*20*).

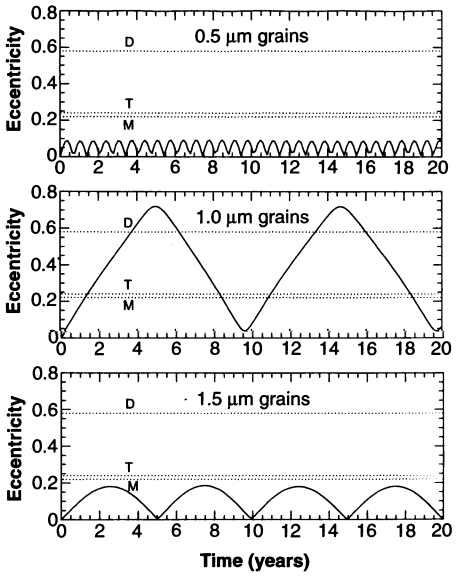

Fig. 2. History of orbital eccentricities for 0.5-, 1.0-, and 1.5-μm particles evolving under oblateness, electromagnetism, and radiation pressure (*2*) as they move about Saturn with orbital semimajor axes of 3.95 R_S. In each case, particles are taken to be icy spheres of density 1.0 g/cm^3 at a potential of −5 V. For 0.5-μm particles, the effect of the Lorentz force dominates the oblateness and the orbit regresses too rapidly for radiation pressure to create substantial eccentricities. For 1.5-μm particles, oblateness dominates, and the orbit precesses swiftly in the opposite direction with the same outcome. For particles 1.0 μm in radius, however, the Lorentz and oblateness precessions approximately cancel, allowing radiation pressure to greatly perturb the orbital eccentricity; a single eccentricity oscillation occurs in one orbital precession period (*2*). The symbols D, T, and M identify the orbital eccentricities at which particles launched from Enceladus will cross the orbits of the neighboring satellites Dione, Tethys, and Mimas, respectively.

Some fraction of E ring material will interact with the interior G, F, and A rings of Saturn (*21–23*). The resulting collisions deplete the E ring and create many small ejecta fragments in the target rings. At the F and G rings, we calculate that the E ring mass flux exceeds the interplanetary mass flux by a factor of 10 to 100; for the outer 100 km of the A ring, this ratio drops to 1 to 10. Regions interior to the outermost A ring are not reached by E ring grains, and so the interplanetary flux dominates there.

Interestingly, tiny particles are unusually plentiful in both the F and G rings. The dustiness of these rings may be augmented by high-velocity impacts of E ring motes into the small particle constituents of the F and G rings. Such collisions are catastrophic and steepen the size distribution. We suggest that the uniquely steep particle size distributions of the F and G rings are determined, in part, by the influx of E ring grains. Furthermore, the outer few hundred kilometers of the A ring are brighter than the ring's inner parts (*23*). The additional flux of E ring particles to the exterior A ring may increase the albedo of large ring members just as impacts may cause the leading versus trailing albedo differences on the major saturnian satellites.

To further test the properties of a self-sustaining E ring, we used a computer simulation containing more sophisticated versions of the simple ideas discussed above. Our model included all of the major moons listed in Table 1; the G, F, and A rings; and seven discrete particle sizes (0.4 to 1.6 μm in steps of 0.2 μm). Before running this simulation, we numerically followed the orbital histories of grains of all sizes launched from each moon and recorded their average inclinations, maximum eccentricities, and the periods of their eccentricity oscillations (Fig. 2). These three parameters were used to approximate the effects of orbital perturbations and hence served as the dynamical inputs to our model.

The collisional yield for a hypervelocity impact into a moon depends only on the target's escape velocity and surface properties and the impactor's kinetic energy (*12*). We assumed that in order to send one projectile-sized fragment into space, the impact energy must exceed the kinetic energy of the escaping fragment by at least a factor of 200. We further considered that the mass of the escaping ejecta scaled with the impact energy, that slightly more mass was ejected in the small size bins than in the large ones, and that intragrain collisions were entirely catastrophic. Finally, individual collision frequencies and yields were folded together with dynamical evolution to calculate a matrix of transition rates (for example, the rate at which 1.2-μm grains from Enceladus created 0.8-μm grains at Tethys). The differential equations governing the population of grains of given sizes associated with specific moons were then numerically integrated (*24*).

The outcome of a typical simulation (Table 2) shows that, as in the actual E ring, most particles in the micrometer-range are localized at Enceladus. Enceladus is selected as the dominant source for several reasons: The nonzero inclinations of its neighbors substantially reduce their collision probabilities (Table 1); the larger escape velocities of Tethys, Dione, and Rhea limit their collisional yields; and Mimas-derived particles are quickly lost to the A, F, and G rings. Besides mimicking the radial structure of the true E ring, our simulated ring has a mass and a peak optical depth within a factor of 3 of the observed values; this agreement reinforces our assertion that intraparticle collisions do in fact determine these quantities.

The only element of our model that stands in contrast to observations is the resulting size distribution, which shows an excess of submicrometer grains rather than being roughly monodisperse at 1 μm (*1*). Better apparent agreement could be forced by an adjustment of the parameters, but without relevant laboratory measurements, there seems little merit in attempting to fine tune the model to reduce its output of submicrometer particles.

Table 2. The final, near steady-state population of a simulated E ring. Each bin was started with a population of 10^{18} particles of the indicated sizes, and the ring's population was followed for 500 years of collisional evolution. The most drastic changes in the population occurred over the first 100 years when grain-grain collisions were rare compared to collisions of ring particles with embedded moons and the G, F, and A rings. The tabulated population has a peak optical depth of about 30% of the true E ring and a cumulative cross-sectional area in ring particles of 1.1 times that of Enceladus. Although we neglect the Lagrangian companions of Tethys and Dione in this simulation for simplicity, their contributions may be important.

Moon	0.4 μm	0.6 μm	0.8 μm	1.0 μm	1.2 μm	1.4 μm	1.6 μm
Mimas	9.3×10^{22}	1.1×10^{22}	1.3×10^{21}	1.4×10^{20}	3.4×10^{20}	2.6×10^{20}	2.5×10^{20}
Enceladus	7.5×10^{22}	4.3×10^{22}	1.1×10^{22}	1.4×10^{21}	1.5×10^{21}	5.6×10^{20}	2.1×10^{20}
Tethys	6.0×10^{22}	9.8×10^{21}	2.1×10^{21}	2.1×10^{19}	3.8×10^{18}	3.6×10^{16}	7.2×10^{14}
Dione	4.9×10^{21}	4.0×10^{20}	5.9×10^{19}	1.1×10^{16}	2.1×10^{14}	3.2×10^{13}	2.5×10^{12}
Rhea	4.7×10^{20}	1.6×10^{18}	4.3×10^{14}	7.7×10^{12}	3.2×10^{11}	0	0
Total	2.3×10^{23}	6.4×10^{22}	1.5×10^{22}	1.6×10^{21}	1.8×10^{21}	8.2×10^{20}	4.6×10^{20}

The relatively large number of small grains is not unexpected dynamically; it follows clearly from our ejecta scaling law and from our assumption that smaller grains are swept up at roughly the same rate as their more massive brethren. Furthermore, because a substantial population of submicrometer dust is observed in the F and G rings, it might be expected in the E ring. Nevertheless, the excess of small particles in the model's output disagrees with the most straightforward interpretation (*1*) of all the observations, namely that the E ring has an appreciably lower optical depth in submicrometer particles than in micrometer grains.

This discrepancy may be partially caused by failings of our dynamical simulation [for example, by incorrect size distributions for the ejecta or underestimated loss rates for submicrometer grains (*25*)]. Nevertheless, we believe that a more likely resolution of this conflict is that submicrometer particles are present, albeit primarily confined to a narrow torus around Enceladus's orbit (Fig. 2). Ground-based measurements of the ring's blue spectrum, which are the strongest constraints to a narrow size distribution, were obtained only for a narrow strip of the E ring. In addition, photometric ratios are based on single images of localized regions. Furthermore, Voyager took only three frames of the E ring's core, near Enceladus' orbit, where our model would suggest small grains should be prevalent; all these images were obtained near a phase angle of 120° and accordingly are not diagnostic of particle size. Under the circumstance where the particle size distribution varies across the ring, as our dynamical model predicts, the photometric modeling technique (*1*), which assumed a single size distribution for the entire ring, may lead to biased results (*26*).

Our model shows how dusty rings, such as Saturn's E ring, may be self-generating. High-velocity impacts into satellites sustain the E ring by generating ejecta, whereas ring particles are lost in catastrophic grain-grain collisions. The resulting steady-state ring has a calculable mass and optical depth that agree with the measured quantities. In general, a self-sustaining ring of this type requires only advantageously located source satellites of proper sizes and a mechanism for increasing the relative velocities between particles and satellites, thereby enhancing collisional yields.

REFERENCES AND NOTES

1. M. R. Showalter, J. N. Cuzzi, S. M. Larson, *Icarus* **94**, 451 (1991).
2. M. Horanyi, J. A. Burns, D. P. Hamilton, *ibid.* **97**, 248 (1992).
3. D. P. Hamilton, *ibid.* **101**, 244 (1993).
4. J. E. P. Connerney, L. Davis Jr., D. L. Chenette, in *Saturn*, T. Gehrels and M. S. Matthews, Eds. (Univ. of Arizona Press, Tucson, AZ, 1984), pp. 354–377.
5. J. A. Burns, P. L. Lamy, S. Soter, *Icarus* **40**, 1 (1979).
6. E. J. Öpik, *Interplanetary Encounters: Close-Range Gravitational Interactions* (Elsevier, New York, 1976).
7. W. A. Feibelman, *Nature* **214**, 793 (1967).
8. K. D. Pang, C. C. Voge, J. W. Rhoads, J. M. Ajello, *J. Geophys. Res.* **89**, 9459 (1984).
9. P. K. Haff, A. Eviatar, G. L. Siscoe, *Icarus* **56**, 426 (1983).
10. W. B. McKinnon, *Lunar Planet. Sci.* **14**, 487 (1983).
11. J. D. O'Keefe and T. J. Ahrens, *Science* **198**, 1249 (1977).
12. Spall fragments, which are only lightly shocked because of cancellation of the initial compressional and the reflected rarefaction stress waves, can exceed the projectile in size. See H. J. Melosh, *Impact Cratering: A Geologic Process* (Oxford Univ. Press, Oxford, 1989).
13. W. Frisch, thesis, Lehrstuhl für Raumfahrttecknik der Technische Universität München, München, Germany (1990).
14. W. Frisch, in *Hypervelocity Impacts in Space*, J. A. M. McDonnell, Ed. (University of Kent at Canterbury, Canterbury, UK, 1992), pp. 7–14.
15. D. Koschny, thesis, Lehrstuhl für Raumfahrt teck-nik der Technische Universität München, München, Germany (1993).
16. A distribution of eccentric orbits having Enceladus' semimajor axis will preferentially strike the leading (trailing) face of exterior (interior) satellites because collisions will occur near apocenter (pericenter). Hence, assuming that impacts cause surface brightening, one can explain why Tethys and Dione, satellites exterior to Enceladus, have brighter leading hemispheres, whereas Mimas, which lies interior to Enceladus, has a brighter trailing hemisphere.
17. B. J. Buratti, *Icarus* **75**, 113 (1988).
18. D. E. Shemansky, P. Matheson, D. T. Hall, H.-Y. Hu, T. M. Tripp, *Nature* **363**, 329 (1993).
19. J. N. Cuzzi and R. H. Durisen, *Icarus* **84**, 467 (1990).
20. D. P. Hamilton and J. A. Burns, *Nature* **365**, 498 (1993); R. E. Johnson *et al.*, *Eos* **74**, 569 (1993).
21. M. R. Showalter and J. N. Cuzzi, *Icarus* **103**, 124 (1993).
22. M. R. Showalter, J. B. Pollack, M. E. Ockert, L. R. Doyle, J. B. Dalton, *ibid.* **100**, 394 (1992).
23. L. Dones, J. N. Cuzzi, M. R. Showalter, *ibid.* **105**, 184 (1993).
24. J. E. Colwell and L. W. Esposito, *ibid.* **86**, 530 (1990).
25. Grains smaller than a few tenths of a micrometer in radius actually gyrate, like electrons and ions, around magnetic field lines. These grains have large velocities relative to circularly orbiting satellites and so they will be swept up more rapidly than we have assumed.
26. The photometric model assumes uniform properties across the ring's expanse, and if that condition is relaxed, the result of a monodisperse size distribution is no longer necessarily valid. Unfortunately, the consequences of relaxing one or another assumption on the derived size distribution are not easily predictable (M. R. Showalter, private communication).
27. J. A. Burns, in *Satellites*, J. A. Burns and M. S. Matthews, Eds. (Univ. of Arizona Press, Tucson, AZ, 1986), pp. 1–38.

28. We thank M. R. Showalter, J. N. Cuzzi, and L. Dones for many useful discussions and acknowledge the assistance of two anonymous reviewers.

17 August 1993; accepted 10 March 1994

Quantum Cascade Laser

Jerome Faist, Federico Capasso,* Deborah L. Sivco, Carlo Sirtori, Albert L. Hutchinson, Alfred Y. Cho

A semiconductor injection laser that differs in a fundamental way from diode lasers has been demonstrated. It is built out of quantum semiconductor structures that were grown by molecular beam epitaxy and designed by band structure engineering. Electrons streaming down a potential staircase sequentially emit photons at the steps. The steps consist of coupled quantum wells in which population inversion between discrete conduction band excited states is achieved by control of tunneling. A strong narrowing of the emission spectrum, above threshold, provides direct evidence of laser action at a wavelength of 4.2 micrometers with peak powers in excess of 8 milliwatts in pulsed operation. In quantum cascade lasers, the wavelength, entirely determined by quantum confinement, can be tailored from the mid-infrared to the submillimeter wave region in the same heterostructure material.

Most solid-state and gas lasers rely on narrow optical transitions connecting discrete energy levels between which population inversion is achieved by optical or electrical pumping (*1*). In contrast, semiconductor diode lasers (*2*), including quantum well lasers (*3*), rely on transitions between energy bands in which conduction electrons and valence band holes, injected into the active layer through a forward-biased *pn* junction, radiatively recombine across the band gap. The band gap essentially determines the emission wavelength (*4*). In addition, because the population inversion is broadly distributed, in accord with Pauli's principle, between bands having dispersion with opposite curvature, the resulting gain spectrum is relatively broad. These characteristics have profound implications for the operation of semiconductor lasers (*3*).

We report the design and demonstration, using molecular beam epitaxy (MBE) (*5*) and band structure engineering (*6*), of a semiconductor injection laser (quantum cascade laser) that differs in a fundamental way from diode lasers. It relies on only one

AT&T Bell Laboratories, Murray Hill, NJ 07974, USA.

*To whom correspondence should be addressed.